

Article

New PVP–Ag or Pd-Doped Perovskite Oxide Hybrid Structures for Water Splitting Electrocatalysis

Adina Căta¹, Bogdan-Ovidiu Țăranu¹ , Ioana Maria Carmen Ienașcu^{1,2} and Paula Sfirloaga^{1,*}

¹ National Institute for Research and Development in Electrochemistry and Condensed Matter, 144 Dr. A. P. Podeanu, 300569 Timisoara, Romania; adina.cata@yahoo.com (A.C.); b.taranu84@gmail.com (B.-O.Ț.); imcienascu@yahoo.com (I.M.C.I.)

² Department of Pharmaceutical Sciences, Faculty of Pharmacy, “Vasile Goldiș” Western University of Arad, 86 Liviu Rebreanu, 310045 Arad, Romania

* Correspondence: paulasfirloaga@gmail.com

Abstract: Global warming and the global energy crisis are two major challenges humanity is currently confronting that are pressuring the scientific community to find efficient, low-cost, and environmentally sustainable solutions. Within this context, hydrogen has emerged as a clean and efficient energy carrier promising to replace environmentally hazardous fossil fuels. The present study, of relevance to the water splitting domain, concerns the synthesis of two novel hybrid structures, namely polyvinylpyrrolidone (PVP) functionalized with Ag-doped LaMnO₃ and Pd-doped LaMnO₃, respectively. The water electrolysis catalytic activity of these new materials was evaluated in a strongly alkaline medium. Perovskite-based modified electrodes were manufactured through four different procedures. The samples displayed electrocatalytic activity for the O₂ evolution reaction and the most active electrode was the one obtained by drop-casting a mixture of LaMnO₃:Ag/PVP and Carbon Black on graphite support. The study is aimed at and succeeds in increasing the scientific database concerning the role of perovskite oxides in the water-splitting field.

Keywords: perovskite oxide; electrocatalyst; water splitting; water electrolysis; oxygen evolution reaction



Citation: Căta, A.; Țăranu, B.-O.; Ienașcu, I.M.C.; Sfirloaga, P. New PVP–Ag or Pd-Doped Perovskite Oxide Hybrid Structures for Water Splitting Electrocatalysis. *Appl. Sci.* **2024**, *14*, 1186. <https://doi.org/10.3390/app14031186>

Academic Editors: Tomasz Pikula and Agata Lisińska-Czekaj

Received: 10 January 2024

Revised: 23 January 2024

Accepted: 29 January 2024

Published: 31 January 2024



Copyright: © 2024 by the authors. Licensee MDPI, Basel, Switzerland. This article is an open access article distributed under the terms and conditions of the Creative Commons Attribution (CC BY) license (<https://creativecommons.org/licenses/by/4.0/>).

1. Introduction

Perovskites represent interesting and promising materials due to advantages such as chemical stability, photostability, low production cost, modifiable energy in the band gap, high absorption properties, as well as long carrier lifetime and diffusion length, which can be used in green and sustainable environmental applications [1]. Despite the high dielectric constant and multifunctionality of perovskite materials, they possess high density, brittleness, and low dielectric strength, as well as poor processability [2].

Polymer–perovskite nanocomposites have attracted the attention of researchers as multifunctional materials for the development of flexible components/devices with many significant technological uses, in which the favorable characteristics of inorganic perovskite nanofiller and organic polymer are effectively integrated [2].

Nanosized filler polymer composites exhibit outstanding properties due to the unique characteristics of nanoparticles, such as the high surface-to-volume ratio and large interfacial area formed between the matrix and nanoparticles, with enhanced mechanical, electrical, and thermal properties. Nanocomposites that combine the advantages of polymer and filler (ceramics) can be processed more easily and are viable alternatives to plain/doped ceramic materials [3].

PVP is a water-soluble, non-toxic amorphous nonionic polymer, with high solubility in polar solvents, widely used in the synthesis of nanoparticles [4] acting as a nanoparticle dispersant, growth modifier, and surface stabilizer, preventing agglomeration of nanoparticles [5]. Due to its amphiphilic nature, PVP can affect the morphology and growth of

nanoparticles by providing solubility in various solvents, discriminative surface stabilization, controlled crystal growth, playing the role of a shape control agent and facilitating the growth of specific crystal faces, while preventing the growth others [5].

Climate change, the worldwide increase in the demand for electricity, and the depletion of the natural resources from which non-renewable energy is obtained are among the major problems facing humanity. In an attempt to resolve these issues, researchers have come to advance environmentally friendly technologies that exploit renewable energy sources and provide energy carriers [6]. Hydrogen is one such energy carrier that has attracted the attention of the scientific community due to its properties, such as its carbon-free composition and very high energy density [6,7]. This gas is currently regarded as an efficient source of environmentally friendly energy that can replace the fossil fuels considered to play a significant role in global warming [8].

There is more than one available technology for generating hydrogen and not all of them are greenhouse gas free. For example, H₂ can be obtained via biomass and fossil fuel burning [9], but in order to avoid damaging the environment the go-to processes are electrolysis and photoelectrolysis [10]. Today, electrochemical water splitting performed by exploiting solar energy either directly or indirectly constitutes a very promising approach for the large-scale generation of hydrogen in an environmentally friendly manner [11,12].

Water electrolysis is a well-known, simple, quick, and non-polluting way of decomposing water molecules into O₂ and H₂ via two main half-reactions: the oxygen and hydrogen evolution reactions (OER and HER) unfolding at the anode and cathode, respectively. If the electricity required by this process is supplied from renewable energy sources—such as solar, wind, and tidal energy—it becomes even more environmentally friendly [13]. One of the issues facing water electrolysis that stands out is constituted by the sluggish reaction kinetics of the OER and HER. To address this problem researchers are aiming to synthesize materials with high electrocatalytic activity for at least one of the two half-reactions. In order to make water splitting viable for large-scale H₂ production the electrocatalysts must also be stable and low cost [14]. Currently, Pt-based catalysts for the HER and Ru- and Ir-based catalysts for the OER are benchmarks when it comes to the performance evaluation of the other catalysts reported in the literature [15–17]. However, their scarcity and high cost are significant obstacles for large-scale applications, making the identification of non-noble materials that are both highly efficient and stable a main concern. The scientific literature contains a large number of functional materials that have been studied regarding their electrocatalytic water-splitting properties, ranging from noble metal-based to non-noble metal-based and metal-free ones [18–20].

Perovskite oxides are a category of functional materials that have been revealed to be very promising for the water-splitting domain [21,22]. These compounds share a crystal structure characterized by the chemical formula ABO₃, where the A-site is occupied by a bigger metal cation than the one occupying the B-site, and they possess properties such as piezoelectricity, superconductivity, ferroelectricity, and enormous magnetoresistivity which make them useful for various industrial and commercial domains [23]. The full potential of perovskite oxides in the water-splitting field has yet to be revealed, but the evaluation of their relevant catalytic properties is of current interest to researchers, as reflected in the recent publications of Sfirloaga et al. [24,25]. In one of the studies, hybrid materials based on montmorillonite functionalized with LaMnO₃ perovskite were obtained for the first time and were tested regarding their water-splitting electrocatalytic activity in alkaline media, which led to the identification of the modified electrode possessing the best properties for the HER [24]. A subsequently published investigation outlines the HER electrocatalytic properties in alkaline media of unsubstituted, Ca-substituted, and Pd-substituted LaMnO₃. The most significant results were obtained for the electrodes modified with compositions containing the Pd-substituted perovskite oxide [25].

The current paper continues the work of Sfirloaga et al. [25] concerning the water electrolysis catalytic properties of perovskite oxide-based modified electrodes via the study of two new materials—LaMnO₃:Ag/PVP (P11) and LaMnO₃:Pd/PVP (P14)—in a strongly

alkaline medium. The modified samples whose OER and HER activity were evaluated experimentally were obtained using four different procedures. The results show that while both perovskite compounds display negligible electrocatalytic activity for the HER, the electrode modified with a composition containing P11 and manufactured with one of the procedures (designated as Procedure 4) is more active toward the OER than the rest of the investigated samples. In terms of novelty, the study of the water-splitting electrocatalytic properties of P11 and P14 has not been previously performed, and the materials have not been previously characterized with the physico-chemical methods mentioned in the paper.

2. Materials and Methods

2.1. Materials and Reagents

Perovskite materials (1% Ag-doped LaMnO_3 and 1% Pd-doped LaMnO_3) were obtained by a previously reported sol-gel technique [26–28]. Nafion solution of 5% concentration was purchased from Sigma Aldrich (Saint Louis, MO, USA) as Nafion[®] 117 and Carbon Black—Vulcan XC 72 was acquired from Fuel Cell Store (Bryan, TX, USA). The role of Nafion was that of binder, enhancing the adhesion of the catalysts and Carbon Black to the substrate, while the use of Carbon Black was aimed at increasing the electron transfer among electrode surface and electroactive species [29]. The glassy carbon (GC) pellets were from Andreescu Labor & Soft SRL (Bucharest, Romania) while the spectroscopic graphite bars (type SW.114, $\varnothing = 6$ mm) were manufactured at the National Corporation “Kablo Bratislava”, the “Electrocarbon Topolcany” factory (Bratislava, Slovakia). Polyvinylpyrrolidone (Sigma-Aldrich), potassium hydroxide (Merck, Darmstadt, Germany), potassium nitrate (Merck), potassium hexacyanoferrate (III) (Sigma-Aldrich), ethanol (Chimreactiv, Bucharest, Romania), and acetone (Chimreactiv) were also used in the study. All aqueous solutions were obtained with double-distilled water produced in the laboratory.

2.2. Synthesis of Hybrid Materials

The procedure for obtaining the new hybrid materials based on polyvinylpyrrolidone (PVP) polymer functionalized with LaMnO_3 type perovskite structures doped with Ag (P11) or Pd (P14) consists of mixing the precursors in a mass ratio of 20:1 (PVP:perovskite) and dispersing them in distilled water. The resulting suspensions were stirred for 2 h maintaining the temperature at 80 °C and 400 rpm using a magnetic stirrer SMHS-3 (Witeg Labortechnik GmbH, Wertheim am Main, Germany). The resulting viscous mixture was cast into a thin film of 2–5 mm thickness on a flat surface (polypropylene film) and dried at room temperature for 12 h. For further analysis, the polymer-perovskite film was triturated until a homogeneous mixture with a small grain size (up to 1 mm) was obtained and then dried in a forced convection oven, at 60 °C for 12 h.

2.3. Characterization of Hybrid Materials

X-ray diffraction (XRD) data were collected using an X'Pert PRO MPD diffractometer (PANalytical, Almelo, The Netherlands) with $\text{Cu-K}\alpha$ radiation in the 2θ range of 10–80°. The ATR-FT-IR spectra were recorded at room temperature in the 4000–600 cm^{-1} range using a Bruker Vertex 70 spectrometer (Bruker Optik GmbH, Rosenheim, Germany) equipped with a Platinum ATR unit, Bruker Diamond A225/Q.1. The morphology of the samples was registered using a scanning electron microscope equipped with energy dispersive X-ray detector (Inspect S + EDAX, FEI, Eindhoven, The Netherlands) in low vacuum mode.

2.4. Procedures for Manufacturing the Modified Electrodes

Four different procedures were employed to obtain the studied modified electrodes. Procedures 1 and 2 involved the use of the GC supports, while graphite was utilized as substrate for the samples obtained with Procedures 3 and 4. The graphite supports were prepared using a previously reported method [25]. Regarding Procedure 1, five suspensions in ethanol were obtained having the compositions presented in Table 1, and were utilized to

manufacture modified electrodes. The general process for electrode construction consisted of taking a volume of 10 μL from one of the suspensions and applying it via the drop-casting method to one of the surfaces of a glassy carbon pellet. When performing the experiments, the dried electrodes were inserted into a polyamide support that ensured a constant geometric surface of 0.28 cm^2 . Concerning Procedure 2, another set of five suspensions was prepared but by the specifications in Table 2. Each modified electrode was manufactured through the same process described in Procedure 1. As for Procedures 3 and 4, they are the same as Procedures 1 and 2 with the exception of the carbon substrate—graphite was used instead of GC.

Table 1. Electrodes obtained with Procedures 1 and 3 and the suspensions used to construct them.

Electrode		Suspension Composition				
Procedure 1	Procedure 3	P11 * (mg)	P14 ** (mg)	Nafion Solution (μL)	Carbon Black (mg)	Ethanol (μL)
GC1 _{CB}	Gr3 _{CB}	-	-	50	5	450
GC1 _{P11}	Gr3 _{P11}	5	-	50	-	450
GC1 _{P11+CB}	Gr3 _{P11+CB}	5	-	100	5	900
GC1 _{P14}	Gr3 _{P14}	-	5	50	-	450
GC1 _{P14+CB}	Gr3 _{P14+CB}	-	5	100	5	900

* PVP functionalized with 1% Ag-doped LaMnO_3 . ** PVP functionalized with 1% Pd-doped LaMnO_3 .

Table 2. Electrodes obtained with Procedures 2 and 4 and the suspensions used to construct them.

Electrode		Suspension Composition				
Procedure 2	Procedure 4	P11 (mg)	P14 (mg)	Nafion Solution (μL)	Carbon Black (mg)	Ethanol (μL)
GC2 _{CB}	Gr4 _{CB}	-	-	50	5	150
GC2 _{P11}	Gr4 _{P11}	5	-	50	-	150
GC2 _{P11+CB}	Gr4 _{P11+CB}	5	-	100	5	300
GC2 _{P14}	Gr4 _{P14}	-	5	50	-	150
GC2 _{P14+CB}	Gr4 _{P14+CB}	-	5	100	5	300

2.5. Electrochemical Experiments

The electrochemical assembly used during the study of the OER and HER electrocatalytic activity of the electrodes constructed with the four procedures consisted of a Voltalab PGZ 402 potentiostat from Radiometer Analytical (Lyon, France), a glass electrolysis cell, an auxiliary plate-type Pt electrode with the geometric surface area of 0.8 cm^2 , the Ag/AgCl (sat. KCl) reference electrode and the working electrode. The role of the working electrode was fulfilled by each of the samples obtained with Procedures 1 to 4, but also by the unmodified glassy carbon and graphite electrodes. The electrolyte employed during the water-splitting experiments was the strongly alkaline 1 M KOH solution. The OER activity of the samples was evaluated by recording anodic linear sweep voltammograms (LSVs) while their HER activity was investigated by tracing cathodic LSVs. The iR -corrected polarization curves were obtained in an unstirred solution at the scan rate (v) of 5 mV/s. Before each HER experiment the electrolyte solution was deaerated by high-purity nitrogen bubbling.

Except if stated differently, the electrochemical potential values (E) are expressed in terms of the Reversible Hydrogen Electrode (RHE) via Equation (1) and the current density values (i) refer to the geometric current density.

The water electrolysis electrocatalytic properties of the electrodes identified as having the highest activity for this process were subjected to additional electrochemical evaluation. Their electrochemically active surface area (ECSA), the diffusion coefficient of hexacyanoferrate (III) ions (D), the values of their Tafel slopes and their stability were studied as

well. The OER overpotential was calculated with Equation (2), and the HER overpotential with Equation (3). The Tafel slope was determined with Equation (4) and the ECSA and D values were estimated using Equation (5)—the Randles–Sevcik equation—together with experimental data obtained from cyclic voltammetry experiments. The voltammetry curves were recorded in 1 M KNO₃ solution, in the absence and presence of 4 mM potassium hexacyanoferrate (III), at increasing scan rate values ($v = 50, 100, 150, 200, 250, 300$ and 350 mV/s) and in the 0–0.8 V potential range vs. Ag/AgCl (sat. KCl).

$$E_{\text{RHE}} = E_{\text{Ag/AgCl(sat. KCl)}} + 0.059 \times \text{pH} + 0.197, \quad (1)$$

$$\eta_{\text{OER}} = E_{\text{RHE}} - 1.23, \quad (2)$$

$$\eta_{\text{HER}} = |E_{\text{RHE}}| - 0 \text{ V}, \quad (3)$$

$$\eta = b \times \log(i) + a, \quad (4)$$

$$I_p = (2.69 \times 10^5) \times n^{3/2} \times A \times D^{1/2} \times C \times v^{1/2} \quad (5)$$

where E_{RHE} = Reversible Hydrogen Electrode potential (V), $E_{\text{Ag/AgCl(sat. KCl)}}$ = potential expressed in terms of the Ag/AgCl (sat. KCl) reference electrode (V), η_{OER} and η_{HER} = O₂ and H₂ evolution overpotentials (V); η = overpotential (V); i = current density (mA/cm²); b = Tafel slope (V/dec); I_p = peak current (A); n = number of electrons involved in the redox process at $T = 298$ K; A = surface of the working electrode (cm²); D = diffusion coefficient of the electroactive species (cm²/s); C = concentration of the electroactive species (M) and v = scan rate (V/s).

Besides Equations [30–32], it is also important to mention that in the case of the ferrocyanide/ferricyanide redox system used in the study, $n = 1$ and D has a theoretical value reported as 6.7×10^{-6} cm²/s [33].

3. Results and Discussion

3.1. XRD Analysis

Figure 1 shows the XRD patterns of the hybrid materials based on polyvinylpyrrolidone (PVP) functionalized with Ag or Pd doped LaMnO₃ type perovskite structures. The structural parameters were refined by fitting the XRD patterns using the Rietveld refinement technique with High Score software was used to investigate the crystalline structure of the new hybrid materials obtained. Thus, the XRD pattern of pure PVP showed two broad characteristic peaks at 2θ of 11.25° and 21.21° , which is in good agreement with results reported by Li et al. [34] and El Hotaby et al. [35]. The obtained hybrid materials present well defined peaks, mainly corresponding to the perovskite phase, which leads to the conclusion that the polymer did not mask the perovskite material.

3.2. FT-IR Analysis

The FT-IR spectra for the precursors (PVP, LaMnO₃:Ag, and LaMnO₃:Pd) and the two hybrid materials (LaMnO₃:Ag/PVP (P11), LaMnO₃:Pd/PVP (P14)) are shown in Figure 2.

The FT-IR spectrum of pure PVA exhibits the following significant absorption bands: 3453 cm⁻¹ related to O-H stretching, 2950 cm⁻¹ corresponding to asymmetric C-H₂ stretching [4,36], 1493 – 1421 cm⁻¹ assigned to C-H₂ deformations [37], 1286 cm⁻¹ attributed to C-N bending vibration from the pyrrolidone structure [38].

A strong absorption peak located at 1652 cm⁻¹ can be assigned to the C=O stretching vibration in the pyrrolidone group [4,36,38,39]. However, Mireles et al. [37] supported the assignment of the peak at ~ 1660 cm⁻¹ as amide I rather than as a carbonyl stretch.

All the major functional groups of the host polymer can be found in the spectra of the hybrid materials. The FT-IR spectra of the hybrid materials show certain differences regarding the position of the absorption bands corresponding to PVP and increased intensities.

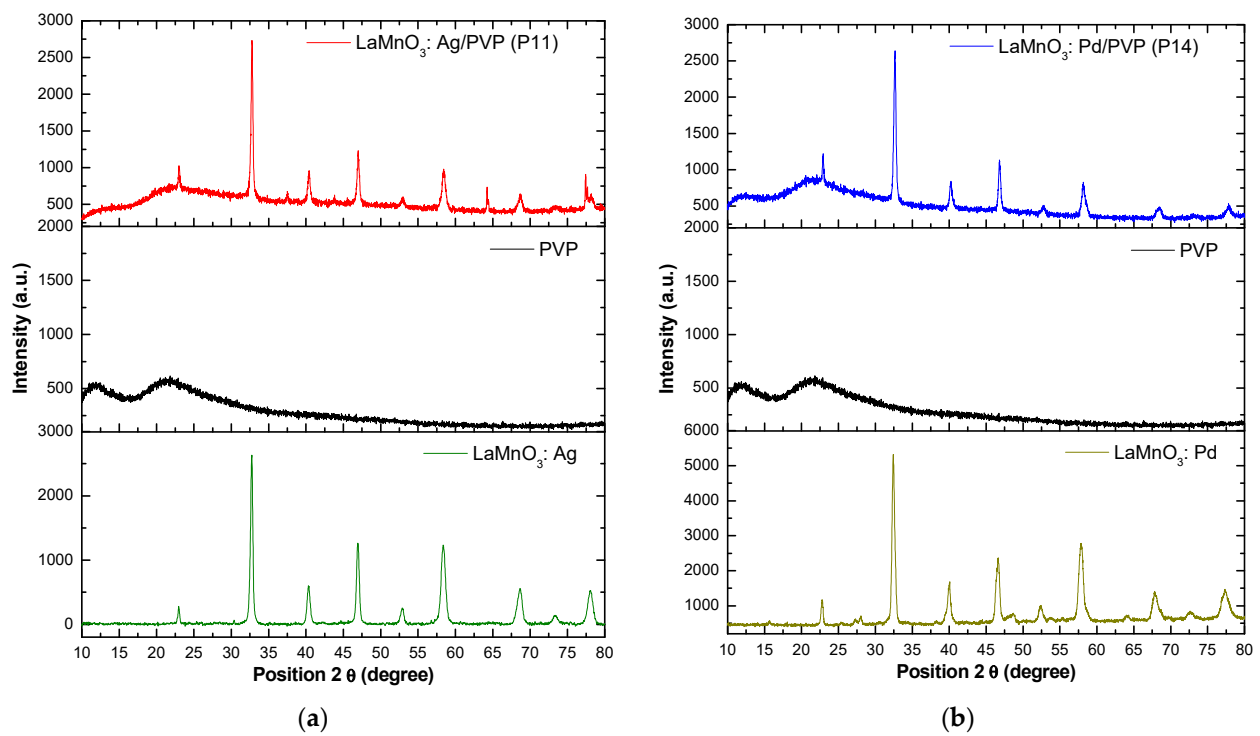


Figure 1. XRD patterns for the precursors and hybrid materials: (a) LaMnO₃:Ag, PVP, and LaMnO₃:Ag/PVP (P11); (b) LaMnO₃:Pd, PVP, and LaMnO₃:Pd/PVP (P14).

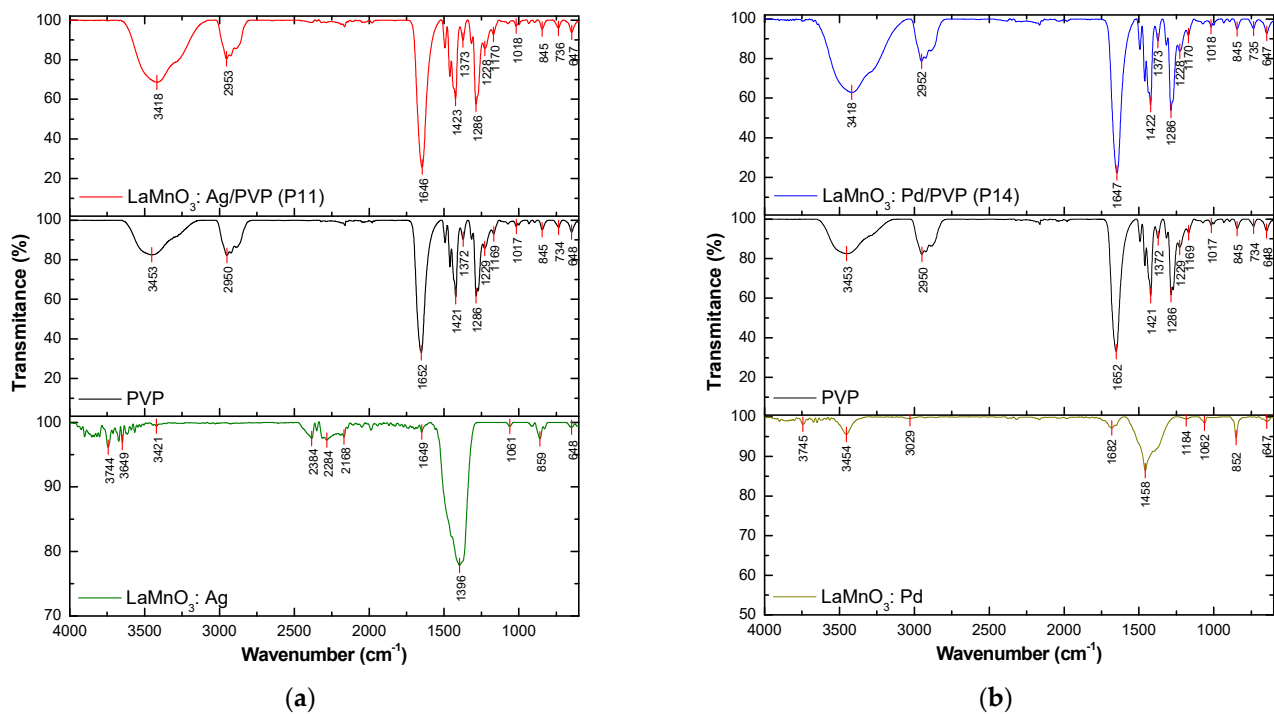


Figure 2. The FT-IR spectra of the precursors and hybrid materials: (a) LaMnO₃:Ag, PVP, and LaMnO₃:Ag/PVP (P11); (b) LaMnO₃:Pd, PVP, and LaMnO₃:Pd/PVP (P14).

The C-H stretching vibration peaks blue-shift to 2953 cm⁻¹ for sample P11, and 2952 cm⁻¹ for sample P14, respectively. The broad band around 3600–3200 cm⁻¹ corresponding to O-H stretching vibration is centered at ~3453 cm⁻¹ in PVP spectra, while in both hybrid materials, it is centered at 3418 cm⁻¹.

The C=O stretching band is shifted from 1652 cm^{-1} to lower wavenumbers in both hybrid materials (1646 cm^{-1} for sample P11, and 1647 cm^{-1} for sample P14). This red shift could be explained by the coordination between metallic species and carbonyl oxygen from PVP [39–41].

The band shifting and their variation in intensities in the FT-IR spectrum indicate the formation of new hybrid materials. The bands of both perovskites are not visible in the spectra of the hybrid materials in the $4000\text{--}600\text{ cm}^{-1}$ range, probably due to the large amount of PVP used compared to the amount of perovskite materials.

3.3. SEM Micrographs

Figure 3 shows the surface morphologies revealed by SEM. Figure 3a presents the qualitative analysis of PVP. As can be seen, the particles have a spherical shape of several tens of micrometers. In the case of perovskite materials doped with Ag or Pd, and functionalized with PVP (Figure 3c,e), it can be observed that the hybrid materials obtained show agglomerations in asymmetric formations. In order to make a comparative study, the SEM images of perovskite materials doped with Ag (Figure 3b) and Pd (Figure 3d) are presented. Thus, it can be seen that perovskite materials have a spherical shape and nanometric sizes.

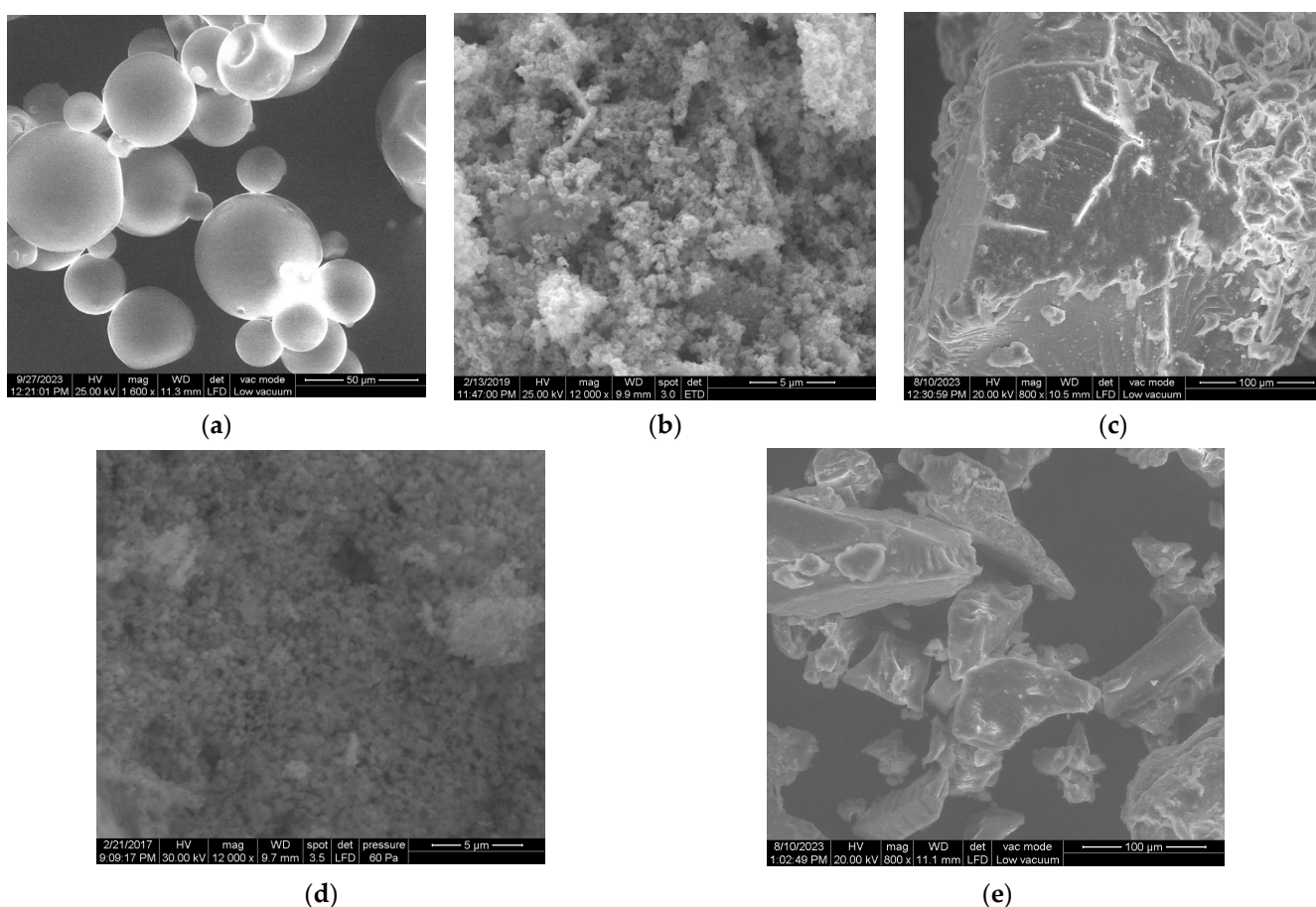


Figure 3. SEM images for (a) PVP; (b) LaMnO₃:Ag; (c) LaMnO₃:Ag/PVP (P11), (d) LaMnO₃:Pd, and (e) LaMnO₃:Pd/PVP (P14).

3.4. Electrochemical Experiments

The OER studies performed on the electrodes modified with Procedure 1 revealed GC1_{P11+CB} and GC1_{P14+CB} as the only samples having higher electrocatalytic activity than the sample modified only with Carbon Black (GC1_{CB}). The polarization curves recorded on these electrodes are shown in Figure 4a. At $i = 10\text{ mA/cm}^2$ —the current density value

at which η_{OER} is usually specified [42–44]— $\eta_{\text{OER}} = 1.145$ V for $\text{GC1}_{\text{P11+CB}}$ and 1.14 V for $\text{GC1}_{\text{P14+CB}}$.

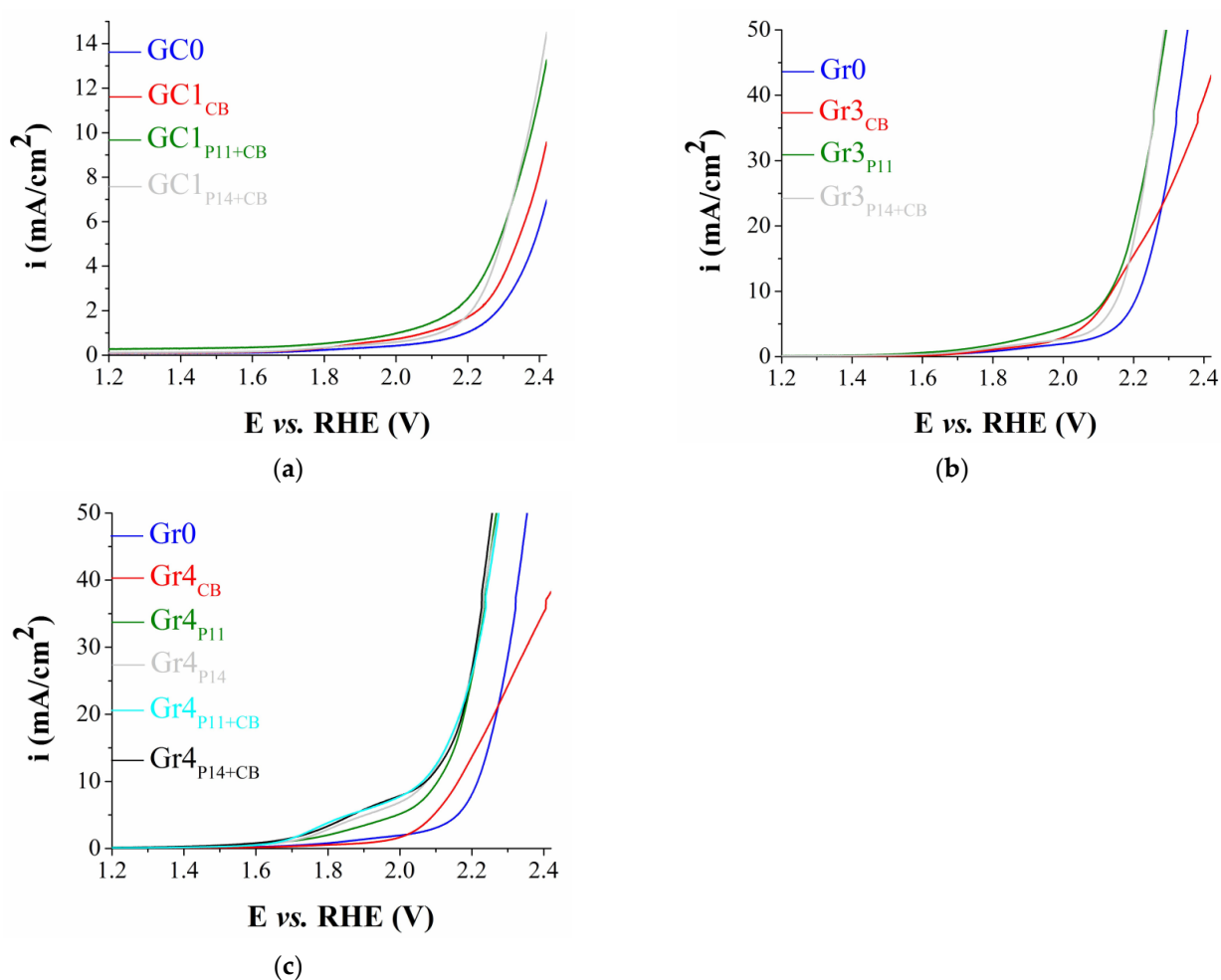


Figure 4. (a) Anodic LSVs recorded on the unmodified glassy carbon electrode (GC0) and on the modified electrodes GC1_{CB} , $\text{GC1}_{\text{P11+CB}}$, and $\text{GC1}_{\text{P14+CB}}$, in 1 M KOH solution, at $v = 5$ mV/s. (b) Anodic polarization curves recorded on the unmodified graphite electrode (Gr0) and on the modified electrodes Gr3_{CB} , Gr3_{P11} , and $\text{Gr3}_{\text{P14+CB}}$, in 1 M KOH solution, at $v = 5$ mV/s. (c) Anodic polarization curves recorded on Gr0, Gr4_{CB} , Gr4_{P11} , Gr4_{P14} , $\text{Gr4}_{\text{P11+CB}}$, and $\text{Gr4}_{\text{P14+CB}}$ electrodes, in 1 M KOH solution, at $v = 5$ mV/s.

The samples obtained using Procedure 1 did not exhibit electrocatalytic activity for the HER, and those obtained by applying Procedure 2 exhibited negligible water-splitting activity. In light of these results subsequent investigations focused only on the OER, and the electrodes manufactured with Procedures 3 and 4 were evaluated in terms of their electrocatalytic activity for this half-reaction.

Figure 4b presents the LSVs recorded on the most catalytically active samples modified using Procedure 3. It can be observed that at current densities >25 mA/cm² the polarization curves traced on Gr3_{P11} and $\text{Gr3}_{\text{P14+CB}}$ overlap, but at lower values of this parameter η_{OER} for the former electrode is $<\eta_{\text{OER}}$ for the latter. However, at $I = 10$ mA/cm², the η_{OER} value determined for the sample obtained using only Carbon Black is higher than for $\text{Gr3}_{\text{P14+CB}}$ and very close to that of Gr3_{P11} (0.91 V vs. 0.9 V). Considering this, the OER catalytic activity of Gr3_{P11} is too low to be considered significant.

The linear voltammograms shown in Figure 4c were traced on the unmodified graphite electrode and on the samples modified according to Procedure 4. Perovskite-containing electrodes exhibited higher OER electrocatalytic activity compared with Gr0 and the Carbon

Black-only modified graphite sample (Gr4_{CB}). At $i = 10 \text{ mA/cm}^2$ $\eta_{\text{OER}} = 0.875 \text{ V}$ for Gr4_{P11}, 0.84 V for Gr4_{P14} and Gr4_{P14+CB}, and 0.83 for Gr4_{P11+CB}. At higher i values, it is observed that the polarization curves are very close to each other and in some cases even overlap.

By comparing the LSVs traced on the perovskite-containing electrodes manufactured via the four procedures it can be concluded that the best results were obtained for the samples resulted by using Procedure 4. Because of the closeness of the η_{OER} values Gr4_{P11}, Gr4_{P14}, Gr4_{P11+CB}, and Gr4_{P14+CB} were all considered for the further evaluation of their electrochemical properties, including their OER electrocatalytic ones. Firstly, their ECSA and the diffusion coefficient of the hexacyanoferrate (III) ions (D) were estimated. To do so, the Randles–Sevcik equation was employed together with data from experiments performed as described in Section 2.5. The obtained values are presented in Table 3.

Table 3. The ECSA and D values were determined in the case of Gr4_{P11}, Gr4_{P14}, Gr4_{P11+CB}, and Gr4_{P14+CB}.

Electrode	ECSA (cm ²)	D (cm ² /s)
Gr4 _{P11}	0.54	2.55×10^{-5}
Gr4 _{P14}	0.74	4.85×10^{-5}
Gr4 _{P11+CB}	1.19	1.21×10^{-4}
Gr4 _{P14+CB}	0.80	5.51×10^{-5}

High values for both parameters are to be desired since a higher D indicates a faster diffusion process while a higher ECSA implies a larger number of catalytic active centers involved in an electrochemical process [45]. As can be seen in Table 3, the highest values were found for the Gr4_{P11+CB} electrode.

The data acquired during the cyclic voltammetry experiments were used to plot the dependence between the peak current densities of the anodic and cathodic peaks corresponding to the ferrocyanide/ferricyanide redox couple and the square root of the scan rate (Figure 5). In all cases, the absolute values of the peak current densities increase proportionally with the scan rate. This increase denotes the specific behavior of diffusion-controlled electron transfer processes [46].

The OER kinetics at the interfaces between the four electrodes and the electrolyte solution were also studied. The obtained Tafel plots are shown in Figure 6, and the determined values of the Tafel slopes can be seen in Table 4. To represent the Tafel curve belonging to each sample the current density was normalized to their estimated ECSA value (i_{ECSA}).

Table 4. Tafel slope values were determined for the Gr4_{P11}, Gr4_{P14}, Gr4_{P11+CB}, and Gr4_{P14+CB} electrodes.

Electrode	Tafel Slope (V/dec)	R ²
Gr4 _{P11}	0.389	0.9996
Gr4 _{P14}	0.247	0.9993
Gr4 _{P11+CB}	0.197	0.9994
Gr4 _{P14+CB}	0.312	0.9995

The smallest Tafel slope value is the one calculated for the Gr4_{P11+CB} sample. A smaller value indicates more favorable kinetics and a higher reaction rate [47].

The electrochemical stability of the four electrodes was evaluated during 7 h chronoamperometric tests at the constant potential value corresponding to $i = 5 \text{ mA/cm}^2$. Gr4_{P11+CB} was revealed to be more stable than the other investigated samples. The i vs. time curves recorded for this electrode and for Gr4_{P14+CB} are presented in Figure 7. In the case of Gr4_{P11+CB}, the i value stabilized at 5.8 mA/cm^2 . LSVs were obtained on this sample before and after the experiment and the results can be seen in Inset a. At higher i values the two polarization curves overlap almost perfectly, but this is not the case at values $< 24 \text{ mA/cm}^2$

where the stability test led to a decrease in the OER activity of the electrode. For example, at $i = 10 \text{ mA/cm}^2$ $\eta_{\text{OER}} = 0.88 \text{ V}$. This 50 mV increase is probably due to the high electrochemical potential applied throughout the chronoamperometric study. Still, the $\text{Gr4}_{\text{P11+CB}}$ electrode was more electrochemically stable than the other samples. To exemplify this, the i vs. time curve recorded under the same conditions but for $\text{Gr4}_{\text{P14+CB}}$ is also included in Figure 7. Apparently, the behavior of the two samples is not very different, but a closer look at the amperogram (Insets b and c) reveals the presence of features attributable to intense alternate processes of O_2 bubble accumulation and release that are not observed on the curve traced on $\text{Gr4}_{\text{P11+CB}}$ [29]. More importantly, once the test ended and the surface of the sample was investigated visually it was observed that the perovskite-containing composition was partially detached from the graphite surface it was deposited on during the manufacturing process.

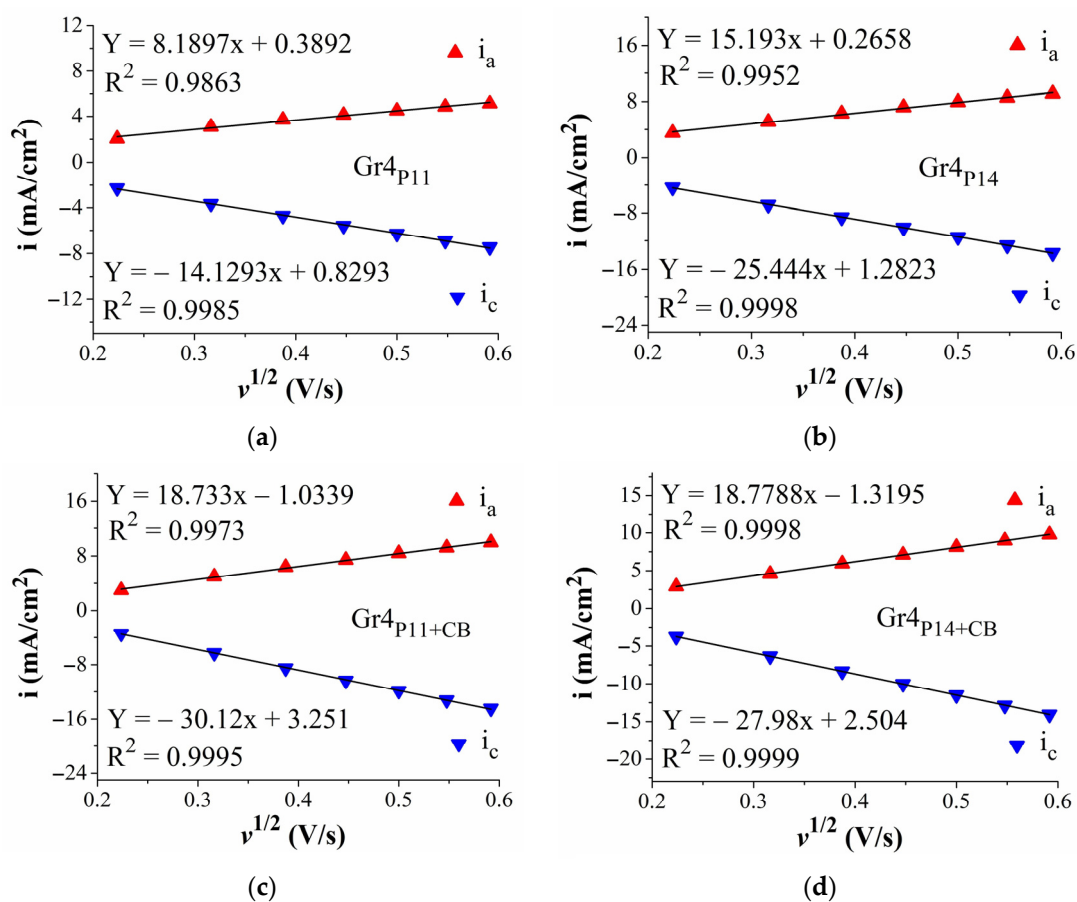


Figure 5. The graphical representation of the dependence between the peak current densities of the anodic and cathodic peaks corresponding to the ferrocyanide/ferricyanide redox couple and the square root of the scan rate for the Gr4_{P11} (a), Gr4_{P14} (b), $\text{Gr4}_{\text{P11+CB}}$ (c), and $\text{Gr4}_{\text{P14+CB}}$ (d) electrodes.

3.5. Further Considerations

The results of the electrochemical experiments evidence the superior properties of the $\text{Gr4}_{\text{P11+CB}}$ electrode. Compared with the Gr4_{P11} , Gr4_{P14} , and $\text{Gr4}_{\text{P14+CB}}$ samples, $\text{Gr4}_{\text{P11+CB}}$ displays higher OER electrocatalytic activity, higher ECSA, and D values, a lower Tafel slope value, and is more electrochemically stable. The higher OER catalytic activity of the electrode modified with the P11 perovskite material, Carbon Black, and Nafion is probably the outcome of structural and transport effects [48]. However, it should also be pointed out that the higher ECSA value estimated for this sample indicates its surface is more discontinuous, probably due to features including edges and defects that generate more catalytically active centers [49]. Furthermore, it is sometimes the case that electrodes manufactured us-

ing compositions containing at least two materials benefits from improved charge transfer and adjusted electron density at the catalytic centers as a result of their interplay [50]. The acquired experimental data implies this is not the case with $\text{Gr4}_{\text{P14}+\text{CB}}$ and $\text{Gr4}_{\text{P11}+\text{CB}}$ which were manufactured using the perovskite oxides mixed with Carbon Black. At $i = -10 \text{ mA/cm}^2$ the η_{OER} values for these samples are very close to those determined for the electrodes obtained without utilizing Carbon Black. This observation is rather unexpected since the material in question was added for electron transfer enhancement purposes. A potential explanation has to do with the way in which the particles constituting the solid phase of the suspension applied on the surface of the carbon substrate were arranged. Arrangements in the shape of thick layers prevent the electrolyte solution from reaching the pores situated deep into the deposited material. The result is a decrease in the number of catalytically active centers that would otherwise participate in the electrochemical reaction [24,51]. According to this explanation, the ECSA values of $\text{Gr4}_{\text{P14}+\text{CB}}$ and $\text{Gr4}_{\text{P11}+\text{CB}}$ could have been higher and the same is true of their OER electrocatalytic activity.

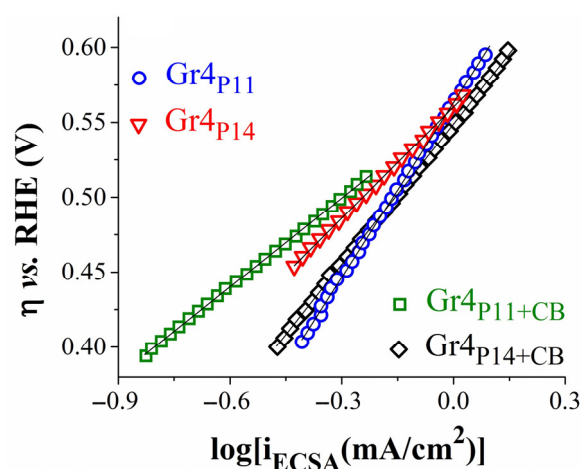


Figure 6. The Tafel plots were obtained for the O_2 evolution reaction on the Gr4_{P11} , Gr4_{P14} , $\text{Gr4}_{\text{P11}+\text{CB}}$, and $\text{Gr4}_{\text{P14}+\text{CB}}$ electrodes, in 1 M KOH solution.

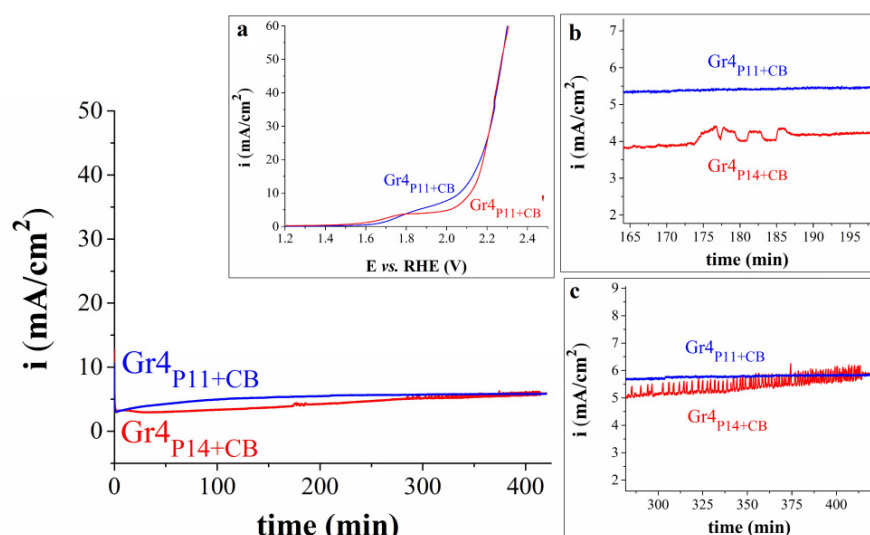


Figure 7. The graphical representation of the dependence between current density and time for the $\text{Gr4}_{\text{P11}+\text{CB}}$ and $\text{Gr4}_{\text{P14}+\text{CB}}$ electrodes immersed in 1 M KOH solution. Insets: (a) The overlap between the polarization curves obtained on the $\text{Gr4}_{\text{P11}+\text{CB}}$ electrode before and after the chronoamperometric experiment, denoted as $\text{Gr4}_{\text{P11}+\text{CB}}$ and $\text{Gr4}_{\text{P11}+\text{CB}}'$, respectively; (b,c) enlarged areas from the overlapped i vs. time curves.

While Gr₄P₁₁+CB possesses superior OER electrocatalytic properties compared with the electrodes investigated during the present study the same cannot be said regarding other electrodes reported in the scientific literature, including other perovskite-based ones [52–55]. The OER catalytic activity of Gr₄P₁₁+CB is not as high and its electrochemical stability is not as good as those of the electrodes from recently published studies. In light of this observation, the future water electrolysis studies that will be performed on P11, P14, and other novel perovskite oxide structures will probably involve a more complex electrode manufacturing method than drop-casting (e.g., pulsed laser deposition and spray pyrolysis).

4. Conclusions

The water electrolysis electrocatalytic properties of two novel perovskite oxides were investigated in a strongly alkaline medium. The perovskite-based electrodes were manufactured using four different procedures. The samples displayed OER activity but negligible HER activity. The electrode obtained by drop-casting a composition containing LaMnO₃:Ag/PVP (P11), Carbon Black, and Nafion on graphite substrate was identified as being the most electrocatalytically active for the OER. Its OER overpotential at $i = 10 \text{ mA/cm}^2$ is 0.83 V, and its Tafel slope is 0.197 V/dec. It was also found to be more electrochemically stable than the other samples.

The present study evaluates for the first time the electrocatalytic properties of new perovskite materials and the obtained results extend the available knowledge of relevance to the water-splitting domain. Furthermore, this work is the first of a series of planned studies and acts as a basis for future OER and HER electrocatalytic activity investigations of other compounds falling under the category of perovskite oxide-based organic–inorganic hybrids.

Author Contributions: Conceptualization, A.C. and P.S.; methodology, A.C. and P.S.; validation, A.C., B.-O.Ț., I.M.C.I. and P.S.; formal analysis, A.C., B.-O.Ț., I.M.C.I. and P.S.; investigation, A.C., B.-O.Ț., I.M.C.I. and P.S.; writing—original draft preparation, A.C., B.-O.Ț. and P.S.; supervision, P.S.; project administration, P.S. All authors have read and agreed to the published version of the manuscript.

Funding: This research received no external funding.

Data Availability Statement: The data presented in this study are available on request from the corresponding author due to privacy.

Acknowledgments: This work was supported by the Experimental Demonstrative Project 683 PED/2022—Executive Unit for Financing Higher Education, Research, Development and Innovation (UEFISCDI). The authors thank D. Ursu, N. S. Tolea, A. Lazar, and C. Moșoarcă from the National Institute of Research and Development for Electrochemistry and Condensed Matter Timisoara for materials characterization.

Conflicts of Interest: The authors declare no conflicts of interest.

References

1. Brahmi, C.; Benlifa, M.; Vaulot, C.; Michelin, L.; Dumur, F.; Airoudj, A.; Morlet-Savary, F.; Raveau, B.; Bousselmi, L.; Lalevée, J. New hybrid perovskites/polymer composites for the photodegradation of organic dyes. *Eur. Polym. J.* **2021**, *157*, 110641. [[CrossRef](#)]
2. Al-Muntaser, A.A.; Pashameah, R.A.; Sharma, K.; Alzahrani, E.; Hameed, S.T.; Morsi, M.A. Boosting of structural, optical, and dielectric properties of PVA/CMC polymer blend using SrTiO₃ perovskite nanoparticles for advanced optoelectronic applications. *Opt. Mater.* **2022**, *132*, 112799. [[CrossRef](#)]
3. Basturk, S.B.; Dancer, C.E.J.; McNally, T. Fabrication and Characterization of Composites of a Perovskite and Polymers with High Dielectric Permittivity. *Mater. Res. Bull.* **2021**, *135*, 111126. [[CrossRef](#)]
4. Koczur, K.M.; Mourdikoudis, S.; Polavarapu, L.; Skrabalak, S.E. Polyvinylpyrrolidone (PVP) in nanoparticle synthesis. *Dalton Trans.* **2015**, *44*, 17883. [[CrossRef](#)]
5. Voronova, M.I.; Surov, O.V.; Rubleva, N.V.; Kochkina, N.E.; Afineevskii, A.V.; Zakharov, A.G. Nanocrystalline cellulose composites with polyvinylpyrrolidone: Selfassembly and dispersibility in water. *Compos. Commun.* **2019**, *15*, 108–112. [[CrossRef](#)]

6. Ahmad, F.; Rafiq, K.; Najam, T.; Hussain, E.; Sohail, M.; Abid, M.Z.; Mahmood, A.; Javed, M.S.; Shah, S.S.A. Metal-organic frameworks for electrocatalytic water-splitting: Beyond the pyrolysis. *Int. J. Hydrogen Energy* **2023**, *48*, 35075–35111. [[CrossRef](#)]
7. Roy, S.; Huang, Z.; Bhunia, A.; Castner, A.; Gupta, A.K.; Zou, X.; Ott, S. Electrocatalytic hydrogen evolution from a cobaloxime-based metal–organic framework thin film. *J. Am. Chem. Soc.* **2019**, *141*, 15942–15950. [[CrossRef](#)] [[PubMed](#)]
8. Hosseini, S.E. Fossil fuel crisis and global warming. In *Fundamentals of Low Emission Flameless Combustion and Its Applications*; Hosseini, S.E., Ed.; Academic Press: London, UK, 2022; pp. 1–11.
9. Lanjekar, P.R.; Panwar, N.L.; Agrawa, C. A comprehensive review on hydrogen production through thermochemical conversion of biomass for energy security. *Bioresour. Technol. Rep.* **2023**, *21*, 101293. [[CrossRef](#)]
10. Bulfin, B.; Carmo, M.; Van de Krol, R.; Mouglin, J.; Ayers, K.; Gross, K.J.; Marina, O.A.; Roberts, G.M.; Stechel, E.B.; Xiang, C. Editorial: Advanced water splitting technologies development: Best practices and protocols. *Front. Energy Res.* **2023**, *11*, 1149688. [[CrossRef](#)]
11. Peng, Y.; Jiang, K.; Hill, W.; Lu, Z.; Yao, H.; Wang, H. Large-scale, low-cost, and high-efficiency water-splitting system for clean H₂ generation. *ACS Appl. Mater. Interfaces* **2019**, *11*, 3971–3977. [[CrossRef](#)]
12. Son, M.-K. Design and demonstration of large scale Cu₂O photocathodes with metal grid structure for photoelectrochemical water splitting. *Energies* **2021**, *14*, 7422. [[CrossRef](#)]
13. Xu, X.; Sun, H.; Jiang, S.P.; Shao, Z. Modulating metal–organic frameworks for catalyzing acidic oxygen evolution for proton exchange membrane water electrolysis. *SusMat* **2021**, *1*, 460–481. [[CrossRef](#)]
14. Wang, S.; Lu, A.; Zhong, C.-J. Hydrogen production from water electrolysis: Role of catalysts. *Nano Converg.* **2021**, *8*, 4. [[CrossRef](#)]
15. Guo, F.; Macdonald, T.J.; Sobrido, A.J.; Liu, L.; Feng, J.; He, G. Recent advances in ultralow-Pt-loading electrocatalysts for the efficient hydrogen evolution. *Adv. Sci.* **2023**, *10*, 2301098. [[CrossRef](#)] [[PubMed](#)]
16. Sun, H.; Jung, W.C. Recent advances in doped ruthenium oxides as high-efficiency electrocatalysts for the oxygen evolution reaction. *J. Mater. Chem. A* **2021**, *9*, 15506–15521. [[CrossRef](#)]
17. Galyamin, D.; Tolosana-Moranchel, A.; Retuerto, M.; Rojas, S. Unraveling the most relevant features for the design of iridium mixed oxides with high activity and durability for the oxygen evolution reaction in acidic media. *JACS Au* **2023**, *3*, 2336–2355. [[CrossRef](#)] [[PubMed](#)]
18. Niu, H.; Wang, Q.; Huang, C.; Zhang, M.; Yan, Y.; Liu, T.; Zhou, W. Noble metal-based heterogeneous catalysts for electrochemical hydrogen evolution reaction. *Appl. Sci.* **2023**, *13*, 2177. [[CrossRef](#)]
19. Li, X.-P.; Huang, C.; Han, W.-K.; Ouyang, T.; Liu, Z.-Q. Transition metal-based electrocatalysts for overall water splitting. *Chin. Chem. Lett.* **2021**, *32*, 2597–2616. [[CrossRef](#)]
20. Zhai, Q.; Pan, Y.; Dai, L. Carbon-based metal-free electrocatalysts: Past, present, and future. *Acc. Mater. Res.* **2021**, *2*, 1239–1250. [[CrossRef](#)]
21. Alom, S.; Kananke-Gamage, C.C.W.; Ramezanipour, F. Perovskite oxides as electrocatalysts for hydrogen evolution reaction. *ACS Omega* **2022**, *7*, 7444–7451. [[CrossRef](#)]
22. Wang, Y.; Wang, L.; Zhang, K.; Xu, J.; Wu, Q.; Xie, Z.; An, W.; Liang, X.; Zou, X. Electrocatalytic water splitting over perovskite oxide catalysts. *Chin. J. Catal.* **2023**, *50*, 109–125. [[CrossRef](#)]
23. Rahman, S.; Hussain, A.; Noreen, S.; Bibi, N.; Arshad, S.; Rehman, J.U.; Tahir, M.B. Structural, electronic, optical and mechanical properties of oxide-based perovskite ABO₃ (A = Cu, Nd and B = Sn, Sc): A DFT study. *J. Solid State Chem.* **2023**, *317*, 123650. [[CrossRef](#)]
24. Taranu, B.-O.; Vlazan, P.; Svera, P.; Poienar, M.; Sfirloaga, P. New functional hybrid materials based on clay minerals for enhanced electrocatalytic activity. *J. Alloys Compd.* **2022**, *892*, 162239. [[CrossRef](#)]
25. Sfirloaga, P.; Taranu, B.-O.; Poienar, M.; Vlazan, P. Addressing electrocatalytic activity of metal-substituted lanthanum manganite for the hydrogen evolution reaction. *Surf. Interfaces* **2023**, *39*, 102881. [[CrossRef](#)]
26. Sfirloaga, P.; Malaescu, I.; Nicolae Marin, C.; Vlazan, P. The effect of partial substitution of Pd in LaMnO₃ polycrystalline materials synthesized by sol–gel technique on the electrical performance. *J. Sol-Gel Sci. Technol.* **2019**, *92*, 537–545. [[CrossRef](#)]
27. Sfirloaga, P.; Vlase, T.; Malaescu, I.; Nicolae Marin, C.; Vlazan, P. Silver doping in lanthanum manganite materials: Structural and electrical properties. *J. Therm. Anal. Calorim.* **2020**, *142*, 1817–1823. [[CrossRef](#)]
28. Sfirloaga, P.; Ivanovici, M.-G.; Poienar, M.; Ianasi, C.; Vlazan, P. Investigation of Catalytic and Photocatalytic Degradation of Methyl Orange Using Doped LaMnO₃ Compounds. *Processes* **2022**, *10*, 2688. [[CrossRef](#)]
29. Zappia, M.I.; Mastronardi, V.; Bellani, S.; Zuo, Y.; Bianca, G.; Gabatel, L.; Gentile, M.; Bagheri, A.; Beydaghi, H.; Drago, F.; et al. Graphene vs. carbon black supports for Pt nanoparticles: Towards next-generation cathodes for advanced alkaline electrolyzers. *Electrochim. Acta* **2023**, *462*, 142696. [[CrossRef](#)]
30. Zhao, Z.; Wu, H.; He, H.; Xu, X.; Jin, Y. Self-standing non-noble metal (Ni–Fe) oxide nanotube array anode catalysts with synergistic reactivity for high-performance water oxidation. *J. Mater. Chem. A* **2015**, *3*, 7179–7186. [[CrossRef](#)]
31. Baciú, A.; Remes, A.; Ilinoiu, E.; Manea, F.; Picken, S.J.; Schoonman, J. Carbon nanotubes composite for environmentally friendly sensing. *Environ. Eng. Manag. J.* **2012**, *11*, 239–246. [[CrossRef](#)]
32. Bard, A.J.; Faulkner, L.R. *Electrochemical Methods: Fundamentals and Applications*, 2nd ed.; John Wiley & Sons: New York, NY, USA, 2001; pp. 186–191.
33. Hrapovic, S.; Liu, Y.; Male, K.B.; Luong, J.H.T. Electrochemical biosensing platforms using platinum nanoparticles and carbon nanotubes. *Anal. Chem.* **2004**, *76*, 1083–1088. [[CrossRef](#)]

34. Li, X.G.; Kresse, I.; Springer, J.; Nissen, J.; Yang, Y.L. Morphology and gas permselectivity of blend membranes of polyvinylpyridine with ethylcellulose. *Polymer* **2001**, *42*, 6859–6869. [[CrossRef](#)]
35. El Hotaby, W.; Sherif, H.H.A.; Hemdan, B.A.; Khalil, W.A.; Khalil, S.K.H. Assessment of in situ-Prepared Polyvinylpyrrolidone-Silver Nanocomposite for Antimicrobial Applications. *Acta Phys. Pol. A* **2017**, *131*, 1554–1560. [[CrossRef](#)]
36. Baganizi, D.R.; Nyairo, E.; Duncan, S.A.; Singh, S.R.; Dennis, V.A. Interleukin-10 Conjugation to Carboxylated PVP-Coated Silver Nanoparticles for Improved Stability and Therapeutic Efficacy. *Nanomaterials* **2017**, *7*, 165. [[CrossRef](#)] [[PubMed](#)]
37. Mireles, L.K.; Wu, M.-R.; Saadeh, N.; Yahia, L.H.; Sacher, E. Physicochemical Characterization of Polyvinyl Pyrrolidone: A Tale of Two Polyvinyl Pyrrolidones. *ACS Omega* **2020**, *5*, 30461–30467. [[CrossRef](#)] [[PubMed](#)]
38. Safo, I.A.; Werheid, M.; Dosche, C.; Oezaslan, M. The role of polyvinylpyrrolidone (PVP) as a capping and structure-directing agent in the formation of Pt nanocubes. *Nanoscale Adv.* **2019**, *1*, 3095. [[CrossRef](#)]
39. Song, Y.-J.; Wang, M.; Zhang, Y.-Y.; Wu, J.-Y.; Zhang, T. Investigation of the role of the molecular weight of polyvinyl pyrrolidone in the shape control of high-yield silver nanospheres and nanowires. *Nanoscale Res. Lett.* **2014**, *9*, 17. [[CrossRef](#)] [[PubMed](#)]
40. Kim, J.H.; Min, B.R.; Kim, C.K.; Won, J.; Kang, Y.S. Spectroscopic Interpretation of Silver Ion Complexation with Propylene in Silver Polymer Electrolytes. *J. Phys. Chem. B* **2002**, *106*, 2786–2790. [[CrossRef](#)]
41. Bryaskova, R.; Daniela Pencheva, D.; Nikolov, S.; Kantardjiev, T. Synthesis and comparative study on the antimicrobial activity of hybrid materials based on silver nanoparticles (AgNps) stabilized by polyvinylpyrrolidone (PVP). *J. Chem. Biol.* **2011**, *4*, 185–191. [[CrossRef](#)] [[PubMed](#)]
42. Menezes, P.W.; Panda, C.; Loos, S.; Bunschei-Bruns, F.; Walter, C.; Schwarze, M.; Deng, X.; Dau, H.; Driess, M. A structurally versatile nickel phosphite acting as a robust bifunctional electrocatalyst for overall water splitting. *Energy Environ. Sci.* **2018**, *11*, 1287–1298. [[CrossRef](#)]
43. Mani, V.; Anantharaj, S.; Mishra, S.; Kalaiselvi, N.; Kundu, S. Iron hydroxyphosphate and Sn-incorporated iron hydroxyphosphate: Efficient and stable electrocatalysts for oxygen evolution reaction. *Catal. Sci. Technol.* **2017**, *7*, 5092–5104. [[CrossRef](#)]
44. Li, J.; Li, J.; Zhou, X.; Xia, Z.; Gao, W.; Ma, Y.; Qu, Y. Highly efficient and robust nickel phosphides as bifunctional electrocatalysts for overall water-splitting. *ACS Appl. Mater. Interfaces* **2016**, *8*, 10826–10834. [[CrossRef](#)]
45. Zhou, Z.; Zaman, W.Q.; Sun, W.; Cao, L.M.; Tariq, M.; Yang, J. Cultivating crystal lattice distortion in IrO₂ via coupling with MnO₂ to boost the oxygen evolution reaction with high intrinsic activity. *Chem. Commun.* **2018**, *54*, 4959–4962. [[CrossRef](#)] [[PubMed](#)]
46. Manea, F.; Pop, A.; Radovan, C.; Malchev, P.; Bebeselea, A.; Burtica, G.; Picken, S.; Schoonman, J. Voltammetric detection of urea on an Ag-modified zeolite-expanded graphite-epoxy composite electrode. *Sensors* **2008**, *8*, 5806–5819. [[CrossRef](#)] [[PubMed](#)]
47. Han, H.S.; Kim, K.M.; Choi, H.; Ali, G.; Chung, K.Y.; Hong, Y.-R.; Choi, J.; Kwon, J.; Lee, S.W.; Lee, J.W.; et al. Parallelized reaction pathway and stronger internal band bending. partial oxidation of metal sulfide–graphene composites: Important factors of synergistic oxygen evolution reaction enhancement. *ACS Catal.* **2018**, *8*, 4091–4102. [[CrossRef](#)]
48. Yanga, B.; Luo, D.; Wua, S.; Zhanga, N.; Ye, J. Nanoscale hetero-interfaces for electrocatalytic and photocatalytic water splitting. *Sci. Technol. Adv. Mater.* **2022**, *23*, 587–616. [[CrossRef](#)]
49. Li, Y.; Wang, H.; Xie, L.; Liang, Y.; Hong, G.; Dai, H. MoS₂ nanoparticles grown on graphene: An advanced catalyst for the hydrogen evolution reaction. *J. Am. Chem. Soc.* **2011**, *133*, 7296–7299. [[CrossRef](#)] [[PubMed](#)]
50. Liu, Y.; Xing, Y.; Zheng, X.; Xu, S.; Li, D.; Jiang, D. Synergistically enhancing electrocatalytic activity of Co₂P by Cr doping and P vacancies for overall water splitting. *Appl. Surf. Sci.* **2022**, *600*, 154099. [[CrossRef](#)]
51. Lahiri, A.; Li, G.; Endres, F. Highly efficient electrocatalytic hydrogen evolution reaction on carbonized porous conducting polymers. *J. Solid State Electrochem.* **2020**, *24*, 2763–2771. [[CrossRef](#)]
52. Tang, J.; Xu, X.; Tang, T.; Zhong, Y.; Shao, Z. Perovskite-Based Electrocatalysts for Cost-Effective Ultrahigh-Current-Density Water Splitting in Anion Exchange Membrane Electrolyzer Cell. *Small Methods* **2022**, *6*, 2201099. [[CrossRef](#)] [[PubMed](#)]
53. Wang, Y.; Jiang, Y.; Zhao, Y.; Ge, X.; Lu, Q.; Zhang, T.; Xie, D.; Li, M.; Bu, Y. Design strategies of perovskite nanofibers electrocatalysts for water splitting: A mini review. *Chem. Eng. J.* **2023**, *451*, 138710. [[CrossRef](#)]
54. Kim, D.; Oh, L.S.; Park, J.H.; Kim, H.J.; Lee, S.; Lim, E. Perovskite-based electrocatalysts for oxygen evolution reaction in alkaline media: A mini review. *Front. Chem.* **2022**, *10*, 1024865. [[CrossRef](#)] [[PubMed](#)]
55. Si, C.; Zhang, W.; Lu, Q.; Guo, E.; Yang, Z.; Chen, J.; He, X.; Luo, J. Recent Advances in Perovskite Catalysts for Efficient Overall Water Splitting. *Catalysts* **2022**, *12*, 601. [[CrossRef](#)]

Disclaimer/Publisher’s Note: The statements, opinions and data contained in all publications are solely those of the individual author(s) and contributor(s) and not of MDPI and/or the editor(s). MDPI and/or the editor(s) disclaim responsibility for any injury to people or property resulting from any ideas, methods, instructions or products referred to in the content.